

APPLIED PHYSICS

Spin-orbit torque manipulated by fine-tuning of oxygen-induced orbital hybridization

Yuito Kageyama¹, Yuya Tazaki¹, Hongyu An¹, Takashi Harumoto², Tenghua Gao¹, Ji Shi², Kazuya Ando^{1,3*}

Current-induced spin-orbit torques provide an effective way to manipulate magnetization in spintronic devices, promising for fast switching applications in nonvolatile memory and logic units. Recent studies have revealed that the spin-orbit torque is strongly altered by the oxidation of heterostructures with broken inversion symmetry. Although this finding opens a new field of metal-oxide spin-orbitronics, the role of the oxidation in the spin-orbit physics is still unclear. Here, we demonstrate a marked enhancement of the spin-orbit torque induced by a fine-tuning of oxygen-induced modification of orbital hybridization. This is evidenced by a concomitant enhancement of the interface spin-orbit torque, interface spin loss, and interface perpendicular magnetic anisotropy within a narrow range of the oxidation level of metallic heterostructures. This result reveals the crucial role of the atomic-scale effects in the generation of the spin-orbit torques, opening the door to atomic-level engineering of the spin-orbit physics.

INTRODUCTION

Oxide electronic materials promise a wide range of applications, such as transparent electronics, optoelectronics, and power harvesting (1). Among this class of materials, Cu oxide is one of the first semiconducting materials to be investigated as early as the 1920s (2). Because of its low cost, good carrier mobility, and direct energy gap, Cu oxide has been used in the fabrication of a variety of electronic devices, including solar cells, resistive switching memories, and transistors (3).

Recently, Cu oxide has become attractive in spin-orbitronics, which aims to discover novel phenomena and functionalities arising from spin-orbit coupling (SOC) (4). The fundamental building block of spin-orbitronics is the generation of spin-orbit torques (SOTs), which enable electric manipulation of magnetization (5–11). Although Cu has been believed to generate negligible SOTs because of the weak SOC, a recent study has shown that Cu becomes an efficient SOT generator through oxidation (12). The oxidation-induced enhancement of the SOTs has been observed in various systems recently (13–16). These findings illustrate the essential role of the oxidation effect in exploring the physics and technology of spin-orbitronics. However, a fundamental understanding of the oxidation effect on the spin-orbit physics is still unclear. The great flexibility of the oxidation level of Cu makes it a model system to study the physics behind the generation of the SOTs manipulated by oxidation.

In this work, we demonstrate that the SOT in spin-orbitronic heterostructures is markedly enhanced through a fine-tuning of oxygen-induced orbital hybridization. By measuring the SOTs for Ni₈₁Fe₁₉/CuO_x bilayers with various oxidation levels, we found that the magnitude of the damping-like (DL) SOT is substantially enhanced, whereas the sign of the field-like (FL) SOT is reversed, only within a narrow range of the oxidation level of CuO_x. We show that this anomaly appears concomitantly with the enhancement of the effective spin-mixing conductance and interface perpendicular magnetic anisotropy (PMA). These results demonstrate the essential role of the atomic-scale

and chemical bonding effects in the interface spin-orbit physics, providing a crucial piece of information for a fundamental understanding of the SOT generation.

RESULTS

Spin-torque ferromagnetic resonance

We used the spin-torque ferromagnetic resonance (ST-FMR) to quantify the SOTs generated by CuO_x films with various oxidation levels. A schematic illustration of the device structure is shown in Fig. 1A. We deposited a Ni₈₁Fe₁₉(10 nm)/CuO_x(10 nm) bilayer, covered by a SiO₂ (4 nm) capping layer, on a SiO₂ substrate by radio frequency (RF) magnetron sputtering, where the numbers in parentheses represent the thickness. For the sputtering of the CuO_x film, we introduced the mixture of argon and oxygen gas into the chamber. The amount of the oxygen gas flow Q in the reactive mixture varied between 0 and 1.5% (see Materials and Methods). As shown in Fig. 1B, the electrical resistivity ρ of the CuO_x film increases markedly with Q , showing that the oxidation level of the CuO_x film is controlled by the oxygen gas flow. The bilayer films were patterned into rectangular strips with a width of 20 μm and length of 150 μm using the photolithography and lift-off techniques. For the ST-FMR measurements, an RF charge current was applied along the longitudinal direction of the device, and an in-plane external magnetic field H was applied with an angle of 45° from the longitudinal direction of the device. In the bilayer, the RF current generates the DL- and FL-SOTs, as well as an Oersted field, driving magnetization precession in the adjacent ferromagnetic Ni₈₁Fe₁₉ layer (17). The magnetization precession induces an oscillation of the resistance in the ferromagnetic layer by the anisotropic magnetoresistance, resulting in the generation of a direct current (DC) voltage V_{mix} through the mixing of the RF charge current and oscillating resistance (18, 19): $V_{\text{mix}} = V_{\text{sym}} W^2 / [(\mu_0 H - \mu_0 H_{\text{FMR}})^2 + W^2] + V_{\text{anti}} W (\mu_0 H - \mu_0 H_{\text{FMR}}) / [(\mu_0 H - \mu_0 H_{\text{FMR}})^2 + W^2]$, where V_{sym} , V_{anti} , and W are the magnitude of the symmetric component, the magnitude of the antisymmetric component, and the spectral width, respectively. H_{FMR} is the ferromagnetic resonance field. Here, in the V_{mix} signal, the symmetric part is proportional to the DL spin-orbit effective field H_{DL} , and the antisymmetric part is due to the sum of the Oersted field H_{Oe} and FL spin-orbit effective field H_{FL} (17). In Fig. 1C, we show the V_{mix}

Copyright © 2019
The Authors, some
rights reserved;
exclusive licensee
American Association
for the Advancement
of Science. No claim to
original U.S. Government
Works. Distributed
under a Creative
Commons Attribution
NonCommercial
License 4.0 (CC BY-NC).

¹Department of Applied Physics and Physico-Informatics, Keio University, Yokohama 223-8522, Japan. ²School of Materials and Chemical Technology, Tokyo Institute of Technology, Tokyo 152-8552, Japan. ³Center for Spintronics Research Network (CSR/N), Keio University, Yokohama 223-8522, Japan.

*Corresponding author. Email: ando@api.keio.ac.jp

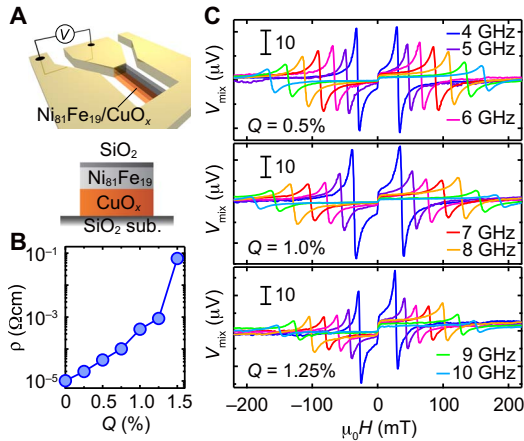


Fig. 1. Spin-torque ferromagnetic resonance. (A) Schematic of the $\text{SiO}_2/\text{Ni}_{81}\text{Fe}_{19}/\text{CuO}_x$ device used for the ST-FMR measurements. To avoid the oxidation of the surface of the $\text{Ni}_{81}\text{Fe}_{19}$ layer, the CuO_x layer was first deposited on a SiO_2 substrate. After the CuO_x deposition, the chamber was evacuated to 1×10^{-6} Pa, and then the $\text{Ni}_{81}\text{Fe}_{19}$ layer was sputtered on top of the CuO_x layer in an Ar atmosphere. Without breaking the vacuum, the surface of the $\text{Ni}_{81}\text{Fe}_{19}$ layer was covered by the SiO_2 capping layer, which was sputtered from a SiO_2 target in an Ar atmosphere. (B) The oxygen flow rate Q dependence of the electrical resistivity ρ , measured by the four-probe method, of the CuO_x films. (C) The magnetic field H dependence of the DC voltage V_{mix} for the $\text{Ni}_{81}\text{Fe}_{19}/\text{CuO}_x$ bilayers with $Q = 0.5, 1.0,$ and 1.25% measured at the RF frequencies from 4 to 10 GHz.

signal for the $\text{Ni}_{81}\text{Fe}_{19}/\text{CuO}_x$ bilayers with $Q = 0.5, 1.0,$ and 1.25% , measured by using a bias tee at room temperature. This result shows that the sign of V_{mix} is reversed by reversing the external magnetic field direction, as expected for the voltage generation induced by the ST-FMR.

Spin-torque generation efficiency

To quantitatively evaluate the influence of the oxidation level of the CuO_x layer on the DL and FL spin-torque efficiencies, we measured the ST-FMR for the $\text{Ni}_{81}\text{Fe}_{19}(d_F)/\text{CuO}_x(10 \text{ nm})$ bilayers with various $\text{Ni}_{81}\text{Fe}_{19}$ layer thicknesses d_F as shown in Fig. 2A. For the bilayers, the FMR spin-torque generation efficiency, $\xi_{\text{FMR}} = (V_{\text{sym}}/V_{\text{anti}})(e\mu_0 M_s d_F d_N / \hbar) \sqrt{1 + M_{\text{eff}}/H_{\text{FMR}}}$, is related to the DL and FL spin-torque efficiencies, ξ_{DL} and ξ_{FL} , as (17)

$$\frac{1}{\xi_{\text{FMR}}} = \frac{1}{\xi_{\text{DL}}} \left(1 + \frac{\hbar}{e \mu_0 M_s d_F d_N} \xi_{\text{FL}} \right) \quad (1)$$

where $\xi_{\text{DL(FL)}} = (2e/\hbar)\mu_0 M_s d_F H_{\text{DL(FL)}}/j_c^N$ (see the Supplementary Materials). Here, j_c^N is the charge current density in the CuO_x layer and d_N is the thickness of the CuO_x layer. M_s and M_{eff} are the saturation magnetization and effective demagnetization field of the $\text{Ni}_{81}\text{Fe}_{19}$ layer, respectively. Using Eq. 1, $\xi_{\text{DL(FL)}}$ can be determined by measuring d_F dependence of ξ_{FMR} under the assumption that $\xi_{\text{DL(FL)}}$ does not have a strong dependence on d_F in the range examined. In Fig. 2B, we show $1/\xi_{\text{FMR}}$ as a function of $1/d_F$ for different Q .

Figure 2B demonstrates that only the bilayer with $Q = 1\%$ shows a different trend in the SOT generation; $1/\xi_{\text{FMR}}$ increases linearly with $1/d_F$ for $Q = 1\%$, whereas $1/\xi_{\text{FMR}}$ decreases linearly with $1/d_F$ for $Q = 0.5, 0.75,$ and 1.25% . The opposite sign of the slope in the linear relation between $1/\xi_{\text{FMR}}$ and $1/d_F$ indicates that the direction

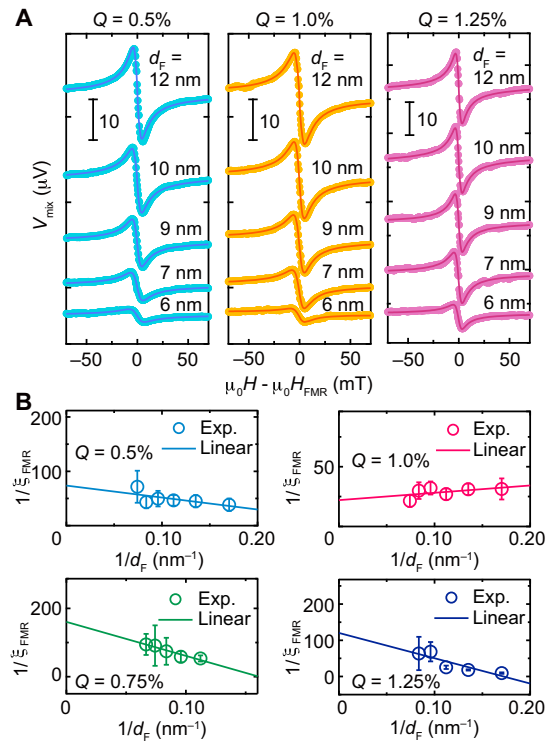


Fig. 2. Thickness dependence of ST-FMR. (A) The ST-FMR spectra for the $\text{Ni}_{81}\text{Fe}_{19}(d_F)/\text{CuO}_x(10 \text{ nm})$ bilayer with $Q = 0.5, 1.0,$ and 1.25% at 7 GHz, where d_F is the thickness of the $\text{Ni}_{81}\text{Fe}_{19}$ layer and H_{FMR} is the ferromagnetic resonance field. The solid circles are the experimental data and the solid curves are the fitting results using the sum of the symmetric and antisymmetric functions. (B) $1/d_F$ dependence of $1/\xi_{\text{FMR}}$ for the devices with different Q . The open circles are the experimental data. The solid lines are the linear fitting results using Eq. 1.

of the FL-SOT generated in the bilayer with $Q = 1\%$ is opposite to that in the bilayer with $Q = 0.5, 0.75,$ and 1.25% (see Eq. 1). We also note that the intercept of the linear fitting of $1/\xi_{\text{FMR}}$ for the bilayer with $Q = 1\%$ is smaller than that for the bilayer with $Q = 0.5, 0.75,$ and 1.25% , indicating a larger DL-SOT generation efficiency when $Q = 1\%$. To study the SOT generation around $Q = 1\%$, we further measured the SOTs by slightly changing Q around 1%. In the following, we discuss the ST-FMR results with respect to the electrical resistivity ρ of the CuO_x layer because ρ changes sensitively and monotonically with Q as shown in Fig. 1B, enabling the characterization of the oxidation level of the CuO_x films.

The drastic change of the SOTs observed in the $\text{Ni}_{81}\text{Fe}_{19}/\text{CuO}_x$ bilayer appears only within a narrow range of the oxidation level. In Fig. 3A, we show the DL and FL spin-torque efficiencies, ξ_{DL} and ξ_{FL} , determined from the $1/d_F$ dependence of $1/\xi_{\text{FMR}}$, as a function of ρ . Figure 3A shows that ξ_{DL} is substantially enhanced only around $\rho = 9 \times 10^{-5} \Omega \text{ cm}$, which is concomitant with the sign reversal of ξ_{FL} . $\xi_{\text{DL}} \sim 0.05$ at $\rho \sim 9 \times 10^{-5} \Omega \text{ cm}$ is comparable to ξ_{DL} for a $\text{Ni}_{81}\text{Fe}_{19}/\text{Pt}$ bilayer, demonstrating efficient SOT generation using CuO_x . Here, the drastic change of the SOTs is irrelevant to phase transformation in the CuO_x layer. The principal phases of Cu oxide are cuprous oxide (Cu_2O) and cupric oxide (CuO). However, from x-ray diffraction and x-ray photoelectron measurements, we found that all the CuO_x films with $Q = 0.50, 0.75, 1.00,$ and 1.25% are a mixture of Cu and Cu_2O ; the CuO phase is absent (see the Supplementary Materials).

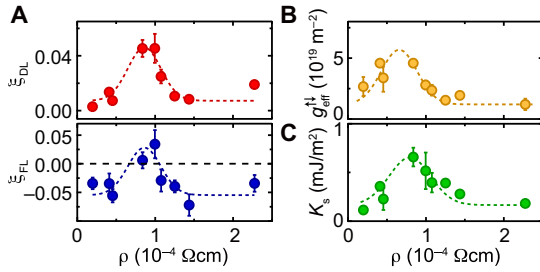


Fig. 3. Spin-torque generation efficiencies. (A) The DL ξ_{DL} and FL ξ_{FL} spin-torque generation efficiencies obtained for the Ni₈₁Fe₁₉/CuO_x bilayers with 0.25% $\leq Q \leq$ 1.25% as a function of the CuO_x layer resistivity ρ . The solid circles are the experimental data, obtained from the $1/d_F$ dependence of $1/\xi_{FMR}$. The dotted curve is a guide for eyes. (B) The effective spin mixing conductance $g_{eff}^{\uparrow\downarrow}$ for the Ni₈₁Fe₁₉/CuO_x bilayers. $g_{eff}^{\uparrow\downarrow}$ was determined from the Ni₈₁Fe₁₉ layer thickness dependence of the magnetic damping constant α . (C) The interface PMA energy density K_s for the Ni₈₁Fe₁₉/CuO_x bilayers. The K_s was determined from d_F dependence of M_{eff} .

DISCUSSION

The marked change of the SOTs is induced by the interface SOC, which is maximized only within the narrow range of the oxidation level. In the moderately oxidized CuO_x ($Q \leq 1.25\%$), both bulk and interface SOC can generate the SOTs because the applied charge current can flow both in the CuO_x bulk and in Ni₈₁Fe₁₉/CuO_x interface layers. The bulk contribution can be eliminated by further increasing the oxidation level of the CuO_x layer because I_c^N/I_c^{tot} decreases with the oxidation, where I_c^N and I_c^{tot} are the charge current flowing in the CuO_x layer and the total charge current flowing in the Ni₈₁Fe₁₉/CuO_x bilayer, respectively. In the bilayer with $\rho \sim 10^{-1} \Omega \text{cm}$ ($Q = 1.5\%$), the resistance of the CuO_x layer is three orders of magnitude larger than that of the Ni₈₁Fe₁₉ layer, and thus the SOTs can only be generated by the interface SOC (see the Supplementary Materials). We note that the sign of the SOTs in the bilayer with $\rho \sim 9 \times 10^{-5} \Omega \text{cm}$, $\xi_{DL} > 0$ and $\xi_{FL} > 0$, is the same as that in the bilayer with $\rho \sim 10^{-1} \Omega \text{cm}$ ($Q = 1.5\%$), where the interface SOC is responsible for the SOTs (see the Supplementary Materials). This indicates that the interface SOC is responsible for the observed anomaly of the SOTs at $\rho \sim 9 \times 10^{-5} \Omega \text{cm}$. This is also supported by the fact that the anomalous SOT disappears by inserting an ultrathin Cu layer between the Ni₈₁Fe₁₉ and CuO_x with $Q = 1\%$ (see the Supplementary Materials). In contrast to the highly oxidized Ni₈₁Fe₁₉/CuO_x bilayer with $\rho \sim 10^{-1} \Omega \text{cm}$, the dominant mechanism of the SOT generation in the bilayer within the resistivity range studied in Fig. 3 is determined by the competition between the bulk and interface SOT generation efficiencies, rather than the spatial distribution of the applied charge current. The reason for this is that the change of I_c^N/I_c^{tot} is not substantial, $I_c^N/I_c^{\text{tot}} \sim 50\%$ for $\rho \sim 9 \times 10^{-5} \Omega \text{cm}$ and $I_c^N/I_c^{\text{tot}} \sim 30\%$ for $\rho \sim 23 \times 10^{-5} \Omega \text{cm}$, and both bulk and interface SOC can generate sizable SOTs in all the films studied in Fig. 3. This indicates that the SOTs can be dominated by the interface SOC only when the interface SOT generation efficiency is substantially higher than that of the bulk SOT generation efficiency in the bilayers studied in Fig. 3. Thus, the sign reversal of the FL-SOT only at $\rho \sim 9 \times 10^{-5} \Omega \text{cm}$ demonstrates that the interface SOT efficiency is markedly enhanced by the oxidation only at $\rho \sim 9 \times 10^{-5} \Omega \text{cm}$, and the dominant mechanism of the SOT generation is changed only around this oxidation level.

The marked enhancement of the interface SOC, within the narrow range of the oxidation level, is further evidenced by angular momentum dissipation from the Ni₈₁Fe₁₉ layer. Figure 3B shows

ρ dependence of the effective spin-mixing conductance $g_{eff}^{\uparrow\downarrow}$, which characterizes the angular momentum dissipation (20). Here, $g_{eff}^{\uparrow\downarrow}$ was obtained from d_F dependence of the magnetic damping constant α (20)

$$\alpha = \alpha_0 + \frac{\gamma \hbar}{4\pi M_s d_F} g_{eff}^{\uparrow\downarrow} \quad (2)$$

where α_0 is the intrinsic magnetic damping of the Ni₈₁Fe₁₉ film and γ is the gyromagnetic ratio. α for the Ni₈₁Fe₁₉/CuO_x bilayers was determined by fitting the microwave frequency f dependence of the ST-FMR spectral width W , using $W = (2\pi\alpha/\gamma)f + W_{\text{ext}}$, where W_{ext} is the inhomogeneous linewidth broadening of the extrinsic contribution (see the Supplementary Materials). Figure 3B shows that $g_{eff}^{\uparrow\downarrow}$ is also enhanced around the oxidation level where ξ_{DL} is maximized and the sign of ξ_{FL} is reversed. In the Ni₈₁Fe₁₉/CuO_x bilayer, $g_{eff}^{\uparrow\downarrow}$ can be associated with the angular momentum absorbed in the bulk and interface: $g_{eff}^{\uparrow\downarrow} = g_{eff}^{\uparrow\downarrow, \text{bulk}} + g_{eff}^{\uparrow\downarrow, \text{int}}$, where the interface contribution, $g_{eff}^{\uparrow\downarrow, \text{int}}$, is known as the spin memory loss due to the interface SOC (21). The bulk contribution is expressed as $g_{eff}^{\uparrow\downarrow, \text{bulk}} = g^{\uparrow\downarrow} [1 + (2e^2/h)(\lambda_N/\sigma_N)g^{\uparrow\downarrow} \coth(d_N/\lambda_N)]^{-1}$, where $g^{\uparrow\downarrow}$ is the bare spin-mixing conductance, and λ_N and σ_N are the spin diffusion length and conductivity of the CuO_x layer, respectively (20). $g_{eff}^{\uparrow\downarrow, \text{bulk}}$ can be changed with the oxidation through the change of $g^{\uparrow\downarrow}$, λ_N , and σ_N . However, the observed change of $g_{eff}^{\uparrow\downarrow}$ can be reproduced by the change of $g_{eff}^{\uparrow\downarrow, \text{bulk}}$ only when we assume $g^{\uparrow\downarrow}$ is negative, which is unphysical. This indicates that the observed enhancement of $g_{eff}^{\uparrow\downarrow}$ is dominated by the enhancement of $g_{eff}^{\uparrow\downarrow, \text{int}}$ or the interface SOC, consistent with the marked change of the interface SOTs.

Our experimental finding is that the SOT is markedly changed through the enhancement of the SOC at the Ni₈₁Fe₁₉/CuO_x interface only within the narrow range of the oxidation level; the interface SOT and SOC are ultrasensitive to the oxidation level of the CuO_x layer. The maximization of the interface SOT through the fine-tuning of the oxidation has not been reported previously. Here, the physics behind the interface SOC, or the Bychkov-Rashba SOC, is the orbital hybridization due to the broken inversion symmetry and atomic SOC. Ab initio calculations show that the strength of the interface SOC is dominated by the asymmetry of the interface-state wave function, or the strength of the hybridization, near the position of the nucleus of the interface atoms in conjunction with the atomic SOC (22–29). Because the orbital hybridization plays a key role in the Rashba physics, several experimental and theoretical studies have proposed that the strength of the Rashba splitting can be tuned by adatom adsorption (28–31).

The critical enhancement of the SOC at the Ni₈₁Fe₁₉/CuO_x interface can be attributed to oxygen-induced deformations of the interface-state wave functions. Since oxygen is an electronegative atom, the charge transfer toward oxygen atoms should be substantial; although O-2p states are weakly spin-orbit-coupled, they can dramatically modify the hybridization of the Ni, Fe, and Cu orbitals near the interface, resulting in the change of the wave-function asymmetry near the nucleus (32). This oxygen-induced wave-function asymmetry can result in the enhancement of the Rashba effect (28). In the Ni₈₁Fe₁₉/CuO_x bilayer, the strength of the atomic SOC of Ni, Fe, and Cu is comparable (33), and thus the wave-function deformation of these atoms near the Ni₈₁Fe₁₉/CuO_x interface can contribute to the observed interface SOC (25). In contrast, since the atomic SOC of O is quite small, the primary

role of the O incorporation is to control the charge distribution, or the orbital hybridization, near the interface (22). We note that the wavefunction deformation near the position of the nucleus of the interface atoms is quite sensitive to the oxygen concentration. An ab initio calculation predicts that the Dzyaloshinskii-Moriya interaction (DMI), which also originates from the interface SOC, is quite sensitive to the atomic-level oxidation; the oxygen incorporation strongly alters the interface DMI through the change of the induced electrostatic dipole moment, or the wavefunction asymmetry, which is suppressed by overoxidation (32). Experimentally, the DMI strength in Pt/Co/metal oxide trilayers has been found to be maximized for the optimum oxidation (34). The maximization of the DMI is consistent with our experimental finding of the enhanced interface SOT within the narrow range of the oxidation level. We also note that the amount of the change in the interface oxidation level of the Ni₈₁Fe₁₉/CuO_x bilayer is reasonable to markedly alter the interface spin-orbit physics. To characterize the Ni₈₁Fe₁₉/CuO_x interface, we have performed x-ray reflectivity (XRR) measurements. The XRR result shows that the thickness d_{NiFeO_x} of the oxidized Ni₈₁Fe₁₉ layer changes systematically with Q in the range of 0.5 to 1.0 nm (see the Supplementary Materials). The range of d_{NiFeO_x} is comparable to the thickness of the oxidized layer of a Pt/Co/Pt structure where a fourfold (an order of magnitude) increase of the DL (FL) torque efficiency was observed by oxidizing the Co layer around $d_{\text{CoO}_x} = 0.5$ nm (15). Here, the anomaly of the SOTs in the Ni₈₁Fe₁₉/CuO_x bilayer cannot be attributed to a possible change of the spin-current absorption due to antiferromagnetic properties of the oxidized interface since the Néel temperature for $d_{\text{NiFeO}_x} < 1$ nm is far below the room temperature (35).

The essential role of the oxygen-induced modification of the orbital hybridization in the critical enhancement of the interface SOT is further supported by a change of the interface PMA. The interface PMA is also known to be the result of orbital hybridization, in combination with the SOC, and is quite sensitive to the interface oxidation level (36). A previous study demonstrated that the PMA at Co/ M interfaces ($M = \text{Al, Mg, and Ta}$) can be optimized through a fine-tuning of the natural oxidation of the interface by controlling the M layer thickness around 0.5 nm (37). To compare the interface SOT and interface PMA, we show the interface PMA energy density K_s for the Ni₈₁Fe₁₉/CuO_x bilayer in Fig. 3C. K_s was determined from d_F dependence of the effective demagnetization field M_{eff} using $\mu_0 M_{\text{eff}} = \mu_0 M_s - 2K_s/(M_s d_F)$, where M_{eff} was obtained using the Kittel formula: $(2\pi f/\gamma) = \sqrt{\mu_0 H_{\text{FMR}}(\mu_0 H_{\text{FMR}} + \mu_0 H_{\text{eff}})}$. Figure 3C shows that the interface PMA is also enhanced at the oxidation level where the anomaly of the SOTs is observed. The concomitant enhancement of the interface SOT and interface PMA demonstrates that the interfacial orbital hybridization, tailored by the oxygen incorporation, governs the spin-orbit physics in the Ni₈₁Fe₁₉/CuO_x bilayer.

In summary, we demonstrated the concomitant enhancement of the interface SOT, interface spin loss, and interface PMA, triggered by the fine-tuning of the interface oxidation level of the Ni₈₁Fe₁₉/CuO_x bilayer. The underlying physics is the marked enhancement of the interface SOC associated with the oxygen-induced modification of the interface orbital hybridization. This mechanism is clearly different from that of the enhanced SOT generated by naturally oxidized Cu, where the bulk effect plays a key role (12). Our results illustrate the essential role of the atomic-scale and chemical bonding effects in the interface spin-orbit physics, providing a way to tune the SOTs by atomic modification (38–40).

MATERIALS AND METHODS

The films were deposited on thermally oxidized Si substrates by RF magnetron sputtering at room temperature. The base pressure in the chamber before the deposition was lower than 1×10^{-6} Pa, and the deposition pressure was 0.2 Pa. The Ni₈₁Fe₁₉ and SiO₂ films were deposited by applying argon gas with a flow rate of 10 standard cubic centimeters per minute (sccm). For the CuO_x deposition, a 99.99% purity Cu target was used, argon gas flow rate was fixed with 20 sccm, and the oxygen gas was applied with the reactive mixture ratio Q . The film thicknesses were controlled by the deposition time with a precalibrated deposition rate for each oxidation level. For the fabrication of the devices used for the ST-FMR experiment, the substrates were patterned into a 20 $\mu\text{m} \times 150 \mu\text{m}$ rectangular shape by standard photolithography before deposition, and lift-off technique was used to take off the remaining part of the films after deposition. For the Ni₈₁Fe₁₉ layer thickness dependence of the ST-FMR, a linear shutter was used to fabricate the Ni₈₁Fe₁₉ layer with various thicknesses. For the x-ray diffraction and x-ray photoelectron measurements of the CuO_x films, the 50-nm-thick films were deposited on glass substrates with different oxygen reactive mixture rates Q by RF magnetron sputtering at room temperature.

SUPPLEMENTARY MATERIALS

Supplementary material for this article is available at <http://advances.sciencemag.org/cgi/content/full/5/11/eaax4278/DC1>

Section S1. Spin-torque efficiency

Section S2. X-ray diffraction and x-ray photoelectron measurements

Section S3. Interface SOTs

Section S4. Spin-torque ferromagnetic resonance for the Ni₈₁Fe₁₉/Cu/CuO_x trilayer

Section S5. Magnetic damping constant

Section S6. Interface oxidation level characterized by x-ray reflectivity

Fig. S1. Characterization of CuO_x films.

Fig. S2. Interface SOTs.

Fig. S3. ST-FMR for trilayer.

Fig. S4. Magnetic damping constant.

Fig. S5. X-ray reflectivity.

Fig. S6. Auger electron spectroscopy.

References (41–44)

REFERENCES AND NOTES

- M. Lorenz, M. S. R. Rao, T. Venkatesan, E. Fortunato, P. Barquinha, R. Branquinho, D. Salgueiro, R. Martins, E. Carlos, A. Liu, F. K. Shan, M. Grundmann, H. Boschker, J. Mukherjee, M. Priyadarshini, N. DasGupta, D. J. Rogers, F. H. Teherani, E. V. Sandana, P. Bove, K. Rietwyk, A. Zaban, A. Veziridis, A. Weidenkaff, M. Muralidhar, M. Murakami, S. Abel, J. Fompeyrine, J. Zuniga-Perez, R. Ramesh, N. A. Spaldin, S. Ostanin, V. Borisov, I. Mertig, V. Lazenka, G. Srinivasan, W. Prellier, M. Uchida, M. Kawasaki, R. Pentcheva, P. Gegenwart, F. M. Granozio, J. Fontcuberta, N. Pryds, The 2016 oxide electronic materials and oxide interfaces roadmap. *J. Phys. D* **49**, 433001 (2016).
- L. O. Grondahl, The copper-cuprous-oxide rectifier and photoelectric cell. *Rev. Mod. Phys.* **5**, 141–168 (1933).
- X. Yu, T. J. Marks, A. Facchetti, Metal oxides for optoelectronic applications. *Nat. Mater.* **15**, 383–396 (2016).
- A. Manchon, J. Železný, I. M. Miron, T. Jungwirth, J. Sinova, A. Thiaville, K. Garello, P. Gambardella, Current-induced spin-orbit torques in ferromagnetic and antiferromagnetic systems. *Rev. Mod. Phys.* **91**, 035004 (2019).
- I. M. Miron, G. Gaudin, S. Auffret, B. Rodmacq, A. Schuhl, S. Pizzini, J. Vogel, P. Gambardella, Current-driven spin torque induced by the Rashba effect in a ferromagnetic metal layer. *Nat. Mater.* **9**, 230–234 (2010).
- L. Liu, C.-F. Pai, Y. Li, H. W. Tseng, D. C. Ralph, R. A. Buhrman, Spin-torque switching with the giant spin Hall effect of tantalum. *Science* **336**, 555–558 (2012).
- J. Kim, J. Sinha, M. Hayashi, M. Yamanouchi, S. Fukami, T. Suzuki, S. Mitani, H. Ohno, Layer thickness dependence of the current-induced effective field vector in Ta[CoFeB]/MgO. *Nat. Mater.* **12**, 240–245 (2013).
- G. Yu, P. Upadhyaya, Y. Fan, J. G. Alzate, W. Jiang, K. L. Wong, S. Takei, S. A. Bender, L.-T. Chang, Y. Jiang, M. Lang, J. Tang, Y. Wang, Y. Tserkovnyak, P. K. Amiri, K. L. Wang,

- Switching of perpendicular magnetization by spin-orbit torques in the absence of external magnetic fields. *Nat. Nanotechnol.* **9**, 548–554 (2014).
9. Y. Fan, P. Upadhyaya, X. Kou, M. Lang, S. Takei, Z. Wang, J. Tang, L. He, L.-T. Chang, M. Montazeri, G. Yu, W. Jiang, T. Nie, R. N. Schwartz, Y. Tserkovnyak, K. L. Wang, Magnetization switching through giant spin-orbit torque in a magnetically doped topological insulator heterostructure. *Nat. Mater.* **13**, 699–704 (2014).
 10. X. Fan, J. Wu, Y. Chen, M. J. Jerry, H. Zhang, J. Q. Xiao, Observation of the nonlocal spin-orbital effective field. *Nat. Commun.* **4**, 1799 (2013).
 11. S. Fukami, C. Zhang, S. DuttaGupta, A. Kurenkov, H. Ohno, Magnetization switching by spin-orbit torque in an antiferromagnet-ferromagnet bilayer system. *Nat. Mater.* **15**, 535–541 (2016).
 12. H. An, Y. Kageyama, Y. Kanno, N. Enishi, K. Ando, Spin-torque generator engineered by natural oxidation of Cu. *Nat. Commun.* **7**, 13069 (2016).
 13. X. Qiu, K. Narayanapillai, Y. Wu, P. Deorani, D.-H. Yang, W.-S. Noh, J.-H. Park, K.-J. Lee, H.-W. Lee, H. Yang, Spin-orbit-torque engineering via oxygen manipulation. *Nat. Nanotechnol.* **10**, 333–338 (2015).
 14. K.-U. Demasius, T. Phung, W. Zhang, B. P. Hughes, S.-H. Yang, A. Kellock, W. Han, A. Pushp, S. S. P. Parkin, Enhanced spin-orbit torques by oxygen incorporation in tungsten films. *Nat. Commun.* **7**, 10644 (2016).
 15. K. Hasegawa, Y. Hibino, M. Suzuki, T. Koyama, D. Chiba, Enhancement of spin-orbit torque by inserting CoO_x layer into Co/Pt interface. *Phys. Rev. B* **98**, 020405 (2018).
 16. H. An, T. Ohno, Y. Kanno, Y. Kageyama, Y. Monnai, H. Maki, J. Shi, K. Ando, Current-induced magnetization switching using an electrically insulating spin-torque generator. *Sci. Adv.* **4**, aar2250 (2018).
 17. C.-F. Pai, Y. Ou, L. H. Vilela-Leão, D. C. Ralph, R. A. Buhrman, Dependence of the efficiency of spin Hall torque on the transparency of Pt/ferromagnetic layer interfaces. *Phys. Rev. B* **92**, 064426 (2015).
 18. L. Liu, T. Moriyama, D. Ralph, R. Buhrman, Spin-torque ferromagnetic resonance induced by the spin Hall effect. *Phys. Rev. Lett.* **106**, 036601 (2011).
 19. W. Zhang, W. Han, X. Jiang, S.-H. Yang, S. S. P. Parkin, Role of transparency of platinum-ferromagnet interfaces in determining the intrinsic magnitude of the spin Hall effect. *Nat. Phys.* **11**, 496–502 (2015).
 20. Y. Tserkovnyak, A. Brataas, G. E. Bauer, B. I. Halperin, Nonlocal magnetization dynamics in ferromagnetic heterostructures. *Rev. Mod. Phys.* **77**, 1375–1421 (2005).
 21. J.-C. Rojas-Sánchez, N. Reyren, P. Laczkowski, W. Savero, J.-P. Attané, C. Deranlot, M. Jamet, J.-M. George, L. Vila, H. Jaffrès, Spin pumping and inverse spin Hall effect in platinum: The essential role of spin-memory loss at metallic interfaces. *Phys. Rev. Lett.* **112**, 106602 (2014).
 22. K. V. Shanavas, Z. S. Popović, S. Satpathy, Theoretical model for Rashba spin-orbit interaction in *d* electrons. *Phys. Rev. B* **90**, 165108 (2014).
 23. M. Hortamani, R. Wiesendanger, Role of hybridization in the Rashba splitting of noble metal monolayers on W(110). *Phys. Rev. B* **86**, 235437 (2012).
 24. L. Petersen, P. Hedegård, A simple tight-binding model of spin-orbit splitting of *sp*-derived surface states. *Surf. Sci.* **459**, 49–56 (2000).
 25. S. Grytsyuk, A. Belabbes, P. M. Haney, H.-W. Lee, K.-J. Lee, M. D. Stiles, U. Schwingenschlögl, A. Manchon, *k*-asymmetric spin splitting at the interface between transition metal ferromagnets and heavy metals. *Phys. Rev. B* **93**, 174421 (2016).
 26. G. Bihlmayer, Y. M. Koroteev, P. Echenique, E. Chulkov, S. Blügel, The Rashba-effect at metallic surfaces. *Surf. Sci.* **600**, 3888–3891 (2006).
 27. S. R. Park, C. H. Kim, J. Yu, J. H. Han, C. Kim, Orbital-angular-momentum based origin of Rashba-type surface band splitting. *Phys. Rev. Lett.* **107**, 156803 (2011).
 28. O. Krupin, G. Bihlmayer, K. Starke, S. Gorovikov, J. E. Prieto, K. Döbrich, S. Blügel, G. Kaindl, Rashba effect at magnetic metal surfaces. *Phys. Rev. B* **71**, 201403 (2005).
 29. H. Tsai, S. Karube, K. Kondou, N. Yamaguchi, F. Ishii, Y. Otani, Clear variation of spin splitting by changing electron distribution at non-magnetic metal/Bi₂O₃ interfaces. *Sci. Rep.* **8**, 5564 (2018).
 30. E. Rotenberg, J. W. Chung, S. D. Kevan, Spin-orbit coupling induced surface band splitting in Li/W(110) and Li/Mo(110). *Phys. Rev. Lett.* **82**, 4066–4069 (1999).
 31. M. Hochstrasser, J. G. Tobin, E. Rotenberg, S. D. Kevan, Spin-resolved photoemission of surface states of W(110)-(1×1)H. *Phys. Rev. Lett.* **89**, 216802 (2002).
 32. A. Belabbes, G. Bihlmayer, S. Blügel, A. Manchon, Oxygen-enabled control of Dzyaloshinskii-Moriya interaction in ultra-thin magnetic films. *Sci. Rep.* **6**, 24634 (2016).
 33. M. Montalti, A. Credi, L. Prodi, M. T. Gandolfi, *Handbook of Photochemistry* (CRC Press, Taylor & Francis Group, 2006).
 34. D. de Souza Chaves, F. Ajejas, V. Křížáková, J. Vogel, S. Pizzini, Oxidation dependence of the Dzyaloshinskii-Moriya interaction in Pt/Co/MO_x trilayers (*M* = Al or Gd). *Phys. Rev. B* **99**, 144404 (2019).
 35. L. Frangou, G. Forestier, S. Auffret, S. Gambarelli, V. Baltz, Relaxation mechanism in NiFe thin films driven by spin angular momentum absorption throughout the antiferromagnetic phase transition in native surface oxides. *Phys. Rev. B* **95**, 054416 (2017).
 36. B. Dieny, M. Chshiev, Perpendicular magnetic anisotropy at transition metal/oxide interfaces and applications. *Rev. Mod. Phys.* **89**, 025008 (2017).
 37. A. Manchon, C. Ducruet, L. Lombard, S. Auffret, B. Rodmacq, B. Dieny, S. Pizzini, J. Vogel, V. Uhliř, M. Hochstrasser, G. Panaccione, Analysis of oxygen induced anisotropy crossover in Pt/Co/MO_x trilayers. *J. Appl. Phys.* **104**, 043914 (2008).
 38. A. Bose, H. Singh, V. K. Kushwaha, S. Bhuktare, S. Dutta, A. A. Tulapurkar, Sign reversal of fieldlike spin-orbit torque in an ultrathin Cr/Ni bilayer. *Phys. Rev. Appl.* **9**, 014022 (2018).
 39. M. Mann, G. S. D. Beach, Reduction of in-plane field required for spin-orbit torque magnetization reversal by insertion of Au spacer in Pt/Au/Co/Ni/Co/Ta. *APL Mater.* **5**, 106104 (2017).
 40. S. Shi, Y. Ou, S. V. Aradhya, D. C. Ralph, R. A. Buhrman, Fast low-current spin-orbit-torque switching of magnetic tunnel junctions through atomic modifications of the free-layer interfaces. *Phys. Rev. Appl.* **9**, 011002 (2018).
 41. V. Tshitoyan, C. Ciccarelli, A. P. Mihal, M. Ali, A. C. Irvine, T. A. Moore, T. Jungwirth, A. J. Ferguson, Electrical manipulation of ferromagnetic NiFe by antiferromagnetic IrMn. *Phys. Rev. B* **92**, 214406 (2015).
 42. M.-H. Nguyen, D. C. Ralph, R. A. Buhrman, Spin torque study of the spin Hall conductivity and spin diffusion length in platinum thin films with varying resistivity. *Phys. Rev. Lett.* **116**, 126601 (2016).
 43. D. D. Stancil, A. Prabhakar, *Spin waves* (Springer, 2009).
 44. S. Hofmann, Sputter depth profile analysis of interfaces. *Rep. Prog. Phys.* **61**, 827 (1998).

Acknowledgments

Funding: This work was supported by JSPS KAKENHI grant numbers 19H00864, 26220604, and 26103004; the Canon Foundation; the Asahi Glass Foundation; the JGC-S Scholarship Foundation; the Kao Foundation for Arts and Sciences; and the Spintronics Research Network of Japan (Spin-RNJ). H.A. acknowledges the support from the JSPS Fellowship (no. P17066). **Author contributions:** Y.K., Y.T., and H.A. fabricated devices and collected and analyzed the data. T.H., T.G., and J.S. performed the materials characterization. K.A. and Y.K. designed the experiments, developed the explanation, and wrote the manuscript. All authors discussed results and reviewed the manuscript. Y.K. claims the responsibility for all the figures in the main text and the Supplementary Materials. **Competing interests:** The authors declare that they have no competing interests. **Data and materials availability:** All data needed to evaluate the conclusions in the paper are present in the paper and/or the Supplementary Materials. Additional data related to this paper may be requested from the authors.

Submitted 22 March 2019

Accepted 17 September 2019

Published 1 November 2019

10.1126/sciadv.aax4278

Citation: Y. Kageyama, Y. Tazaki, H. An, T. Harumoto, T. Gao, J. Shi, K. Ando, Spin-orbit torque manipulated by fine-tuning of oxygen-induced orbital hybridization. *Sci. Adv.* **5**, eaax4278 (2019).